First, rough measurements of spatial resolution were made using wires. Figure 5 shows a radiogram of a 200-μm-diameter tungsten wire coiled around a pipe made of polymethyl methacrylate. In this radiography, the wire was observed with blurring, and image quality improved with increases in the x-ray duration. Next, two radiograms of a metronome are shown in Fig. 6, and stop-motion images of a pendulum are visible. In radiography of plastic bullets, spherical bullets were clearly observed (Fig. 7). Finally, the image of water falling into a polypropylene beaker from a plastic test tube is shown in Fig. 8. This image was taken with the slight addition of an iodine-based contrast medium. Because the x-ray duration was 1 ms, the stop-motion image of water could be obtained.

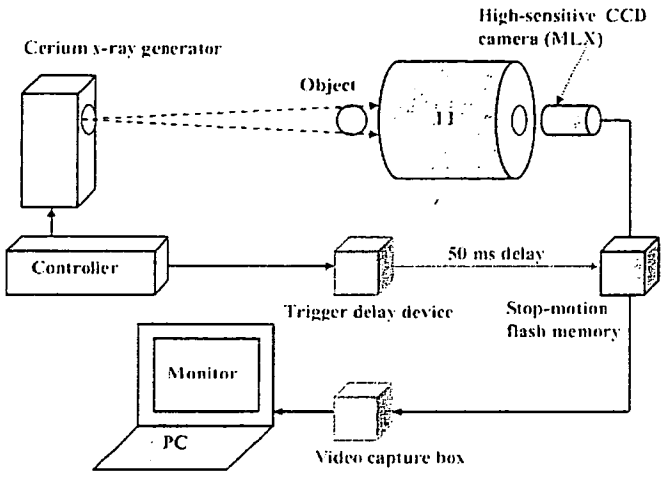


Fig. 4. Experimental setup for performing real-time radiography utilizing the MLX camera.

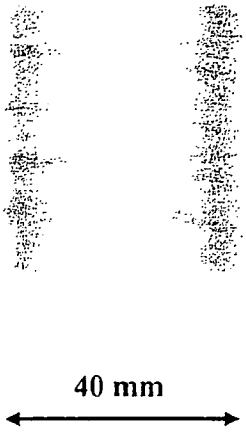


Fig. 5. Radiogram of a 200-μm-diameter tungsten wire coiled around a pipe made of polymethyl methacrylate.

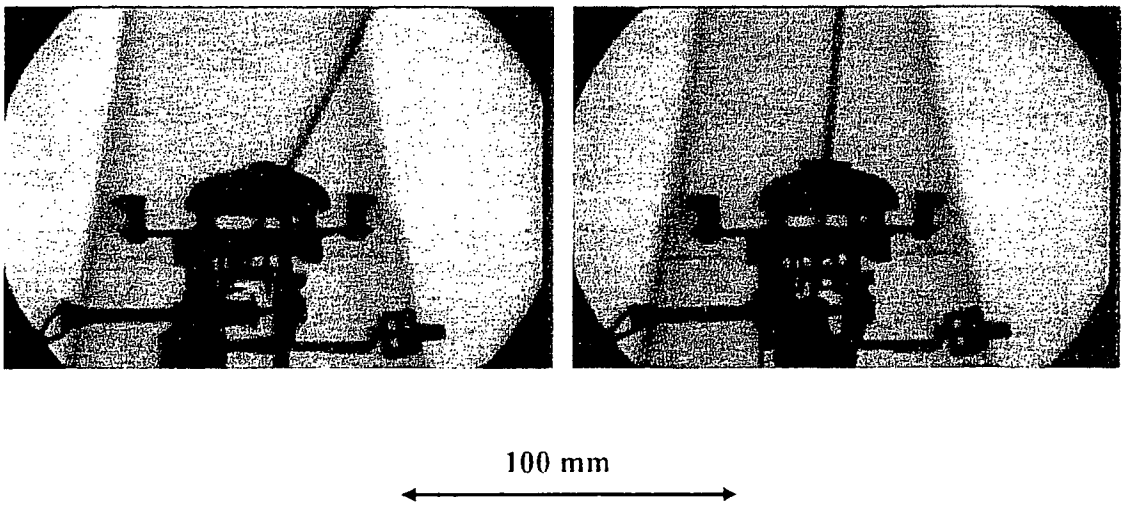


Fig. 6. Two radiograms of a metronome.

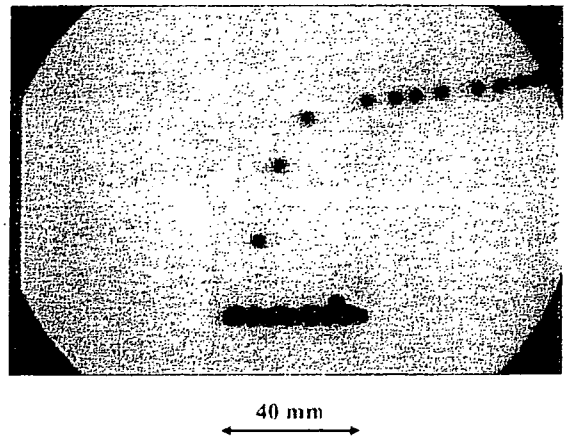


Fig. 7. Radiogram of plastic bullets falling into a polypropylene beaker from a plastic test tube.

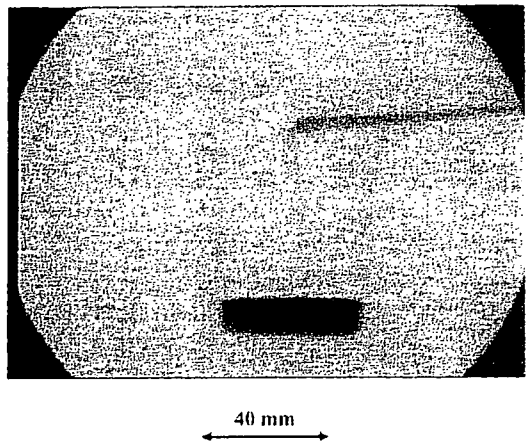


Fig. 8. Radiogram of water falling into a polypropylene beaker from a plastic test tube using an iodine medium.

## 5. DISCUSSION

We performed a fundamental study on the intensification of the x-ray image signal using the MLX camera, and the image quality improved with increases in the x-ray duration. The spatial resolution was primarily determined by the resolution of I I and the pixel number of the camera. Therefore, the resolution improves with improving the I I resolution and with increasing the pixel number.

Without considering the absorbed dose, short-duration real-time radiography is possible by decreasing the image capture time of the camera using a steady-state x-ray generator. In cases where a microfocus x-ray generator is employed, the spatial resolution improves using magnification radiography, and the real-time radiography with a capture time of 1 ms can be performed by image intensifying.

In this experiment, although we performed only single-shot radiography, high-speed dynamic radiography could be possible using a high-speed high-sensitive video camera synchronizing to the repetitive x-ray output, and the repetition rate can be increased to approximately 50 kHz.

## ACKNOWLEDGMENTS

This work was supported by Grants-in-Aid for Scientific Research (13470154, 13877114, 16591181, and 16591222) and Advanced Medical Scientific Research from MECSST, Health and Labor Sciences Research Grants (RAMT-nano-001, RHGTEFB-genome-005 and RHGTEFB-saisei-003), Grants from The Keiryo Research Foundation, The Promotion and Mutual Aid Corporation for Private Schools of Japan, Japan Science and Technology Agency (JST), and the New Energy and Industrial Technology Development Organization (NEDO, Industrial Technology Research Grant Program in '03).

## REFERENCES

1. A. Mattsson, "Some characteristics of a 600 kV flash x-ray tube," *Physica Scripta*, **5**, 99-102, 1972.
2. R. Germer, "X-ray flash techniques," *J. Phys. E: Sci. Instrum.*, **12**, 336-350, 1979.
3. E. Sato, S. Kimura, S. Kawasaki, H. Isobe, K. Takahashi, Y. Tamakawa and T. Yanagisawa, "Repetitive flash x-ray generator utilizing a simple diode with a new type of energy-selective function," *Rev. Sci. Instrum.*, **61**, 2343-2348, 1990.

4. A. Shikoda, E. Sato, M. Sagae, T. Oizumi, Y. Tamakawa and T. Yanagisawa, "Repetitive flash x-ray generator having a high-durability diode driven by a two-cable-type line pulser," *Rev. Sci. Instrum.*, **65**, 850-856, 1994.
5. E. Sato, K. Takahashi, M. Sagae, S. Kimura, T. Oizumi, Y. Hayasi, Y. Tamakawa and T. Yanagisawa, "Sub-kilohertz flash x-ray generator utilizing a glass-enclosed cold-cathode triode," *Med. & Biol. Eng. & Comput.*, **32**, 289-294, 1994.
6. K. Takahashi, E. Sato, M. Sagae, T. Oizumi, Y. Tamakawa and T. Yanagisawa, "Fundamental study on a long-duration flash x-ray generator with a surface-discharge triode," *Jpn. J. Appl. Phys.*, **33**, 4146-4151, 1994.
7. E. Sato, Y. Hayasi, R. Germer, E. Tanaka, H. Mori, T. Kawai, T. Ichimaru, K. Takayama and H. Ido, "Quasi-monochromatic flash x-ray generator utilizing weakly ionized linear copper plasma," *Rev. Sci. Instrum.*, **74**, 5236-5240, 2003.
8. E. Sato, Y. Hayasi, R. Germer, E. Tanaka, H. Mori, T. Kawai, T. Ichimaru, S. Sato, K. Takayama and H. Ido, "Sharp characteristic x-ray irradiation from weakly ionized linear plasma," *J. Electron Spectrosc. Related Phenom.*, **137-140**, 713-720, 2004.
9. E. Sato, M. Sagae, E. Tanaka, Y. Hayasi, R. Germer, H. Mori, T. Kawai, T. Ichimaru, S. Sato, K. Takayama and H. Ido, "Quasi-monochromatic flash x-ray generator utilizing a disk-cathode molybdenum tube," *Jpn. J. Appl. Phys.*, **43**, 7324-7328, 2004.
10. E. Sato, E. Tanaka, H. Mori, T. Kawai, S. Sato and K. Takayama, "Clean monochromatic x-ray irradiation from weakly ionized linear copper plasma," *Opt. Eng.*, **44**, 049002-1-6, 2005.
11. E. Sato, E. Tanaka, H. Mori, T. Kawai, T. Ichimaru, S. Sato, K. Takayama and H. Ido, "Compact monochromatic flash x-ray generator utilizing a disk-cathode molybdenum tube," *Med. Phys.*, **32**, 49-54, 2005.
12. E. Sato, Y. Hayasi, R. Germer, E. Tanaka, H. Mori, T. Kawai, T. Inoue, A. Ogawa, S. Sato, T. Ichimaru, K. Takayama, J. Onagawa and H. Ido, "Monochromatic flash x-ray generator utilizing a disk-cathode silver tube," *Opt. Eng.*, **44**, 096501-1-6, 2005.
13. E. Sato, Y. Hayasi, K. Kimura, E. Tanaka, H. Mori, T. Kawai, T. Inoue, A. Ogawa, S. Sato, K. Takayama, J. Onagawa and H. Ido, "Enhanced K-edge angiography utilizing tantalum plasma x-ray generator in conjunction with gadolium-based contrast media," *Jpn. J. Appl. Phys.*, **44**, 8716-8721, 2005.
14. E. Sato, Y. Hayasi, R. Germer, K. Kimura, E. Tanaka, H. Mori, T. Kawai, T. Inoue, A. Ogawa, S. Sato, K. Takayama and H. Ido, "Enhanced K-edge plasma angiography achieved with tungsten Kα rays utilizing gadolinium-based contrast media," *SPIE*, **5920**, 592012-1-8, 2005.
15. E. Sato, Y. Hayasi, R. Germer, E. Tanaka, H. Mori, T. Kawai, T. Inoue, A. Ogawa, S. Sato, K. Takayama, J. Onagawa, "X-ray spectra from weakly ionized linear copper plasma," *Jpn. J. Appl. Phys.*, **45**, 5301-5306, 2006.
16. E. Sato, E. Tanaka, H. Mori, T. Kawai, T. Inoue, A. Ogawa, S. Sato, K. Takayama and J. Onagawa, "Characteristic x-ray generator utilizing angle dependence of bremsstrahlung x-ray distribution," *Jpn. J. Appl. Phys.*, **45**, 2845-2849, 2006.
17. E. Sato, E. Tanaka, H. Mori, T. Kawai, S. Sato, H. Ojima, K. Takayama and H. Ido, "Energy selective high-speed radiography utilizing stroboscopic x-ray generator," *SPIE*, **5580**, 765-771, 2005.
18. E. Sato, Y. Hayasi, R. Germer, K. Kimura, E. Tanaka, H. Mori, T. Kawai, T. Inoue, A. Ogawa, S. Sato, K. Takayama and H. Ido, "Energy-selective gadolinium angiography utilizing a stroboscopic x-ray generator," SPIE, **5920**, 59200V-1-8, 2005.
*dresato@iwate-med.ac.jp; phone +81-19-651-5111; fax +81-19-654-9282

# K-edge magnification digital angiography using a 100-$\mu$m-focus tungsten tube

**Eiichi Sato,** MEMBER SPIE
Iwate Medical University
Department of Physics
Morioka 020-0015, Japan

**Etsuro Tanaka**
Tokyo University of Agriculture
Department of Nutritional Science
Faculty of Applied Bioscience
Setagaya-ku 156-8502, Japan

**Hidezo Mori**
National Cardiovascular Center Research Institute
Department of Cardiac Physiology
Osaka 565-8565, Japan

**Hiroki Kawakami**
**Toshiaki Kawai,** MEMBER SPIE
Hamamatsu Photonics K. K.
Electron Tube Division 2
Iwata 438-0193, Japan

**Takashi Inoue**
**Akira Ogawa**
Iwate Medical University
Department of Neurosurgery
School of Medicine
Morioka 020-8505, Japan

**Mitsuru Izumisawa**
Iwate Medical University
Department of Oral Radiology
School of Dentistry
Morioka 020-0021, Japan

**Kiyomi Takahashi**
**Shigehiro Sato**
Iwate Medical University
Department of Microbiology
School of Medicine
Morioka 020-8505, Japan

**Kazuyoshi Takayama,** MEMBER SPIE
Tohoku University
Shock Wave Research Center
Institute of Fluid Science
Sendai 980-8577, Japan

**Jun Onagawa**
Tohoku Gakuin University
Department of Applied Physics and Informatics
Faculty of Engineering
Tagajo 985-8537, Japan

**Abstract.** A microfocus x-ray tube is useful to perform magnification digital radiography, including phase-contrast effects. The 100-$\mu$m-focus x-ray generator consists of a main controller for regulating the tube voltage and current, and a tube unit with a high-voltage circuit and a fixed anode x-ray tube. The maximum tube voltage, current, and electric power are 105 kV, 0.5 mA, and 50 W, respectively. Using a 3-mm-thick aluminum filter, the x-ray intensity is 26.0 $\mu$Gy/s at 1.0 m from the source, with a tube voltage of 60 kV and a current of 0.50 mA. Because the peak photon energy is approximately 35 keV using the filter with a tube voltage of 60 kV, the bremsstrahlung x-rays are absorbed effectively by iodine-based contrast media with an iodine K-edge of 33.2 keV. Magnification angiography is performed by threefold magnification imaging with a computed radiography system using iodine-based microspheres 15 $\mu$m in diameter. In angiography of nonliving animals, we observe fine blood vessels approximately 100 $\mu$m with high contrasts.

[DOI: 10.1117/1.2542285]

Subject terms: High-contrast angiography; magnification digital radiography; microfocus x-ray tube; energy-selective imaging; phase-contrast effect.

Paper 051014R received Dec. 27, 2005; revised manuscript received Aug. 9, 2006; accepted for publication Aug. 10, 2006; published online Mar. 2, 2007. This paper is a revision of a paper presented at the SPIE conference on Laser-Generated, Synchrotron, and Other Laboratory X-Ray and EUV Sources, Optics, and Applications II, Aug. 2005, San Diego, California. The paper presented there appears (unrefereed) in SPIE Proceedings Vol. 5918.

## 1 Introduction

Conventional flash x-ray generators utilizing condensers in conjunction with cold-cathode tubes are useful to perform high-speed radiography, including biomedical applications, and several different generators have been developed.[1–7] In particular, linear-plasma x-ray generators[8–10] utilizing triodes have been employed to produce clean K-series characteristic x-rays of nickel and copper, and we have confirmed the irradiation of higher harmonic hard x-rays of K-series characteristic x-rays. Without forming plasmas, a flash x-ray diode with a disk cathode can be employed to perform a fundamental study on producing characteristic x-rays,[11,12] and we have succeeded in producing clean K-series lines using the angle dependence of bremsstrahlung x-ray distribution in Sommerfeld's theory. However, monochromatic flash radiography has had difficulties in increasing x-ray duration and in performing magnification radiography, including the phase-contrast effect.

0091-3286/2007/$25.00 © 2007 SPIE

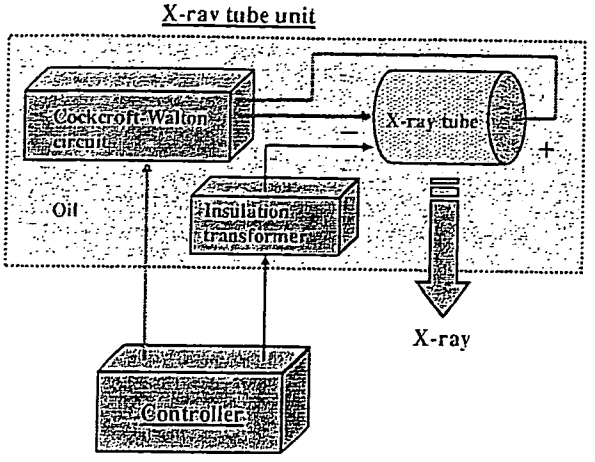


Fig. 1 Block diagram of the x-ray generator.

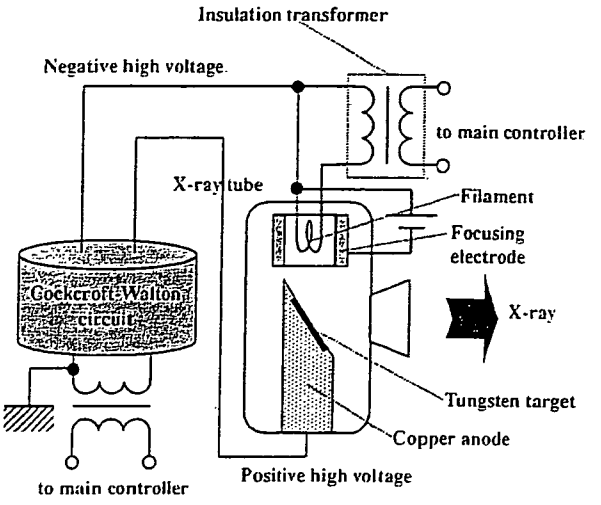


Fig. 2 Electric circuit of the x-ray generator.

Synchrotrons are capable of producing high-dose-rate monochromatic parallel x-ray beams using a monochrocollimator, and the beams have been applied to phase-contrast radiography[13,14] and enhanced K-edge angiography.[15,16] In angiography, monochromatic x-rays with photon energies approximately 35 keV have been employed, because the rays are absorbed effectively by iodine-based contrast media with an iodine K edge of 33.2 keV.

Without using synchrotrons, phase-contrast radiography for edge enhancement can be performed using a microfocus x-ray tube. Magnification radiography, including the phase-contrast effect, has been applied in mammography achieved with a computed radiography (CR) system[17] using a 100-$\mu$m-focus molybdenum tube.[18] Subsequently, we have developed a cerium x-ray generator[19,20] to perform enhanced K-edge angiography using cone beams, and have succeeded in observing fine blood vessels and coronary arteries with high contrasts using cerium K$\alpha$ rays of 34.6 keV. However, it is difficult to design a small focus cerium tube for angiography.

Magnification radiography is useful to improve the spatial resolution in digital radiography, and the phase contrast may come into effect in edge enhancement of comparatively large objects, including thick blood vessels filled with low-density contrast media. Therefore, narrow-photon-energy bremsstrahlung x-rays with a peak energy of approximately 35 keV from a microfocus tungsten tube are useful to perform high-contrast high-resolution angiography.

In the present research, we employed a 100-$\mu$m-focus tungsten tube, used to perform enhanced magnification angiography by controlling bremsstrahlung x-ray spectra using an aluminum filter.

## 2 Experimental Setup

Figure 1 shows the block diagram of a microfocus x-ray generator used in this experiment, and the generator consists of a main controller, an x-ray tube unit with a Cockcroft-Walton circuit, an insulation transformer, and a 100-$\mu$m-focus x-ray tube. The tube voltage, current, and exposure time can be controlled by the controller. The main circuit for producing x-rays is illustrated in Fig. 2, and employs the Cockcroft-Walton circuit to decrease the dimensions of the tube unit. In the x-ray tube, positive and negative high voltages are applied to the anode and cathode electrodes, respectively. The filament heating current is supplied by an AC power supply in the controller, in conjunction with an insulation transformer, which is used for isolation from the high voltage from the Cockcroft-Walton circuit. In this experiment, the tube voltage applied was from 45 to 70 kV, and the tube current was regulated to within 0.50 mA (maximum current) by the filament temperature. The exposure time is controlled to obtain optimum x-ray intensity, and narrow-photon-energy bremsstrahlung x-rays are produced using a 3.0-mm-thick aluminum filter for absorbing soft x-rays.

## 3 Results and Discussion

### 3.1 *X-Ray Intensity*

The x-ray intensity was measured by a Victoreen 660 ionization chamber 1.0 m from the x-ray source using the filter (Fig. 3). At a constant tube current of 0.50 mA, the x-ray

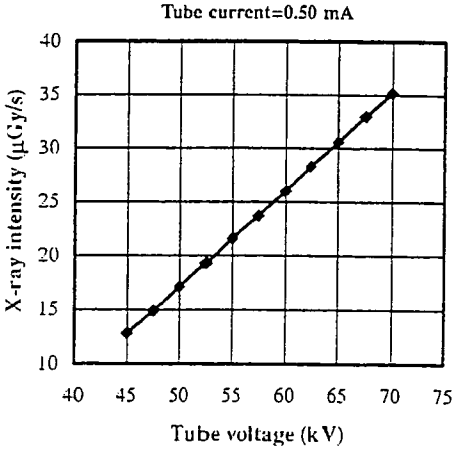


Fig. 3 X-ray intensity ($\mu$Gy/s) as a function of tube voltage (kV) with a tube current of 0.50 mA.

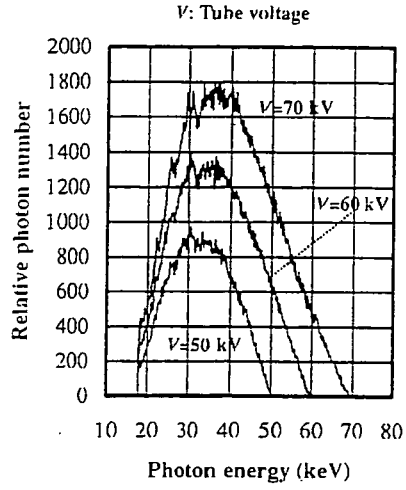


Fig. 4 Bremsstrahlung x-ray spectra measured using a cadmium telluride detector with changes in the tube voltage.

intensity increased when the tube voltage was increased. At a tube voltage of 60 kV, the intensity with the filter was 26.0 $\mu$Gy/s.

### 3.2 *X-Ray Spectra*

To measure x-ray spectra, we employed a cadmium telluride detector (XR-100T, Amptek) (Fig. 4). When the tube voltage was increased, the bremsstrahlung x-ray intensity increased, and both the maximum photon energy and the spectrum peak energy increased.

To perform K-edge angiography, bremsstrahlung x-rays of approximately 35 keV are useful, and the high-energy bremsstrahlung x-rays decrease the image contrast. Using this filter, because bremsstrahlung x-rays with energies higher than 60 keV were not absorbed easily, the tube voltage for angiography was determined as 60 kV by considering the filtering effect of radiographic objects.

### 3.3 *Magnification Radiography*

Magnification radiography was performed by threefold magnification imaging using the CR system and the filter at a tube voltage of 60 kV. The distance between the x-ray source and the imaging plate was 1.5 m (Fig. 5). First, the spatial resolutions of conventional (cohesion) and magnification radiographies were made using a lead test chart. In the magnification radiography, 62.5-$\mu$m lines (eight line pairs) were visible (Fig. 6). Subsequently, Fig. 7 shows radiograms of tungsten wires coiled around rods made of

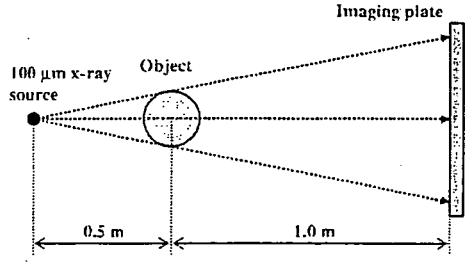


Fig. 5 Threefold magnification imaging using an imaging plate in conjunction with a microfocus tube.

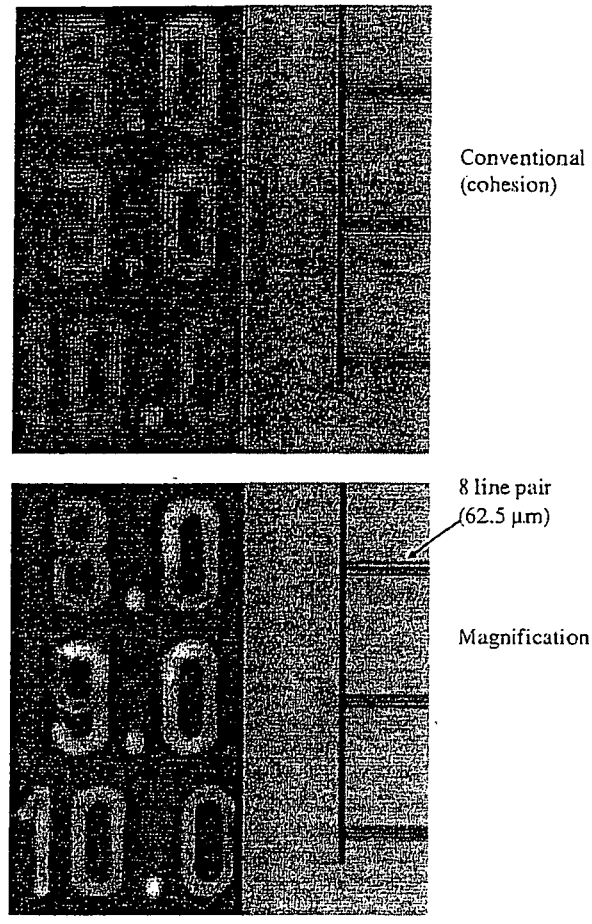


Fig. 6 Radiograms of a test chart for measuring the spatial resolution.

polymethyl methacrylate (PMMA). Although the image contrast decreased somewhat with decreases in the wire diameter, due to blurring of the image caused by the sampling pitch of 87.5 $\mu$m, a 50-$\mu$m-diam wire could be observed. Radiograms of one set of a bolt and a nut are shown in Fig. 8. The edge of a bubble in the bolt and the seam between the bolt and the nut are visible in magnification radiography.

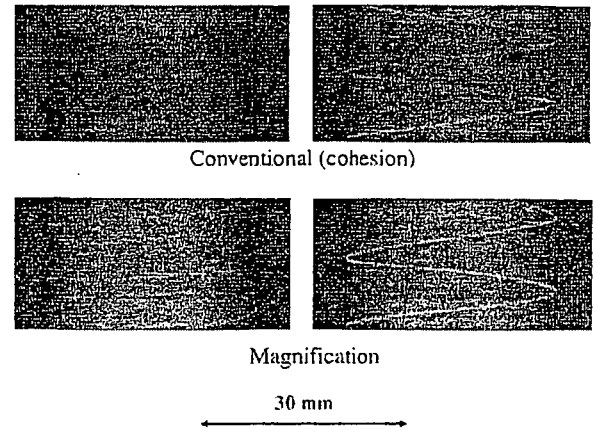


Fig. 7 Radiograms of tungsten wires coiled around PMMA rods.

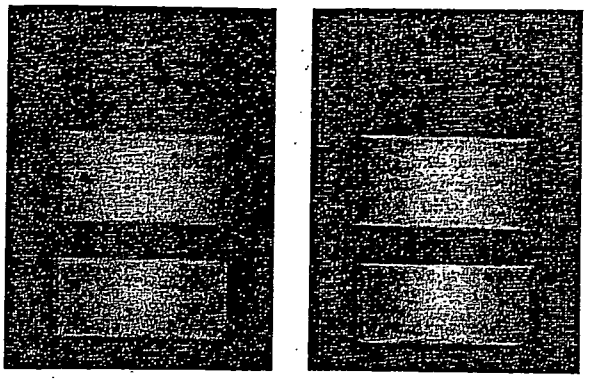


Fig. 8 Radiograms of a plastic bolt and nut.

### 3.4 *Enhanced Magnification Angiography*

Figure 9 shows the mass attenuation coefficients of iodine at the selected energies; the coefficient curve is discontinuous at the iodine K edge. The effective bremsstrahlung x-ray spectra for K-edge angiography are shown above the iodine K edge. Because iodine contrast media with a K-absorption edge of 33.2 keV absorb the rays easily, blood vessels were observed with high contrasts.

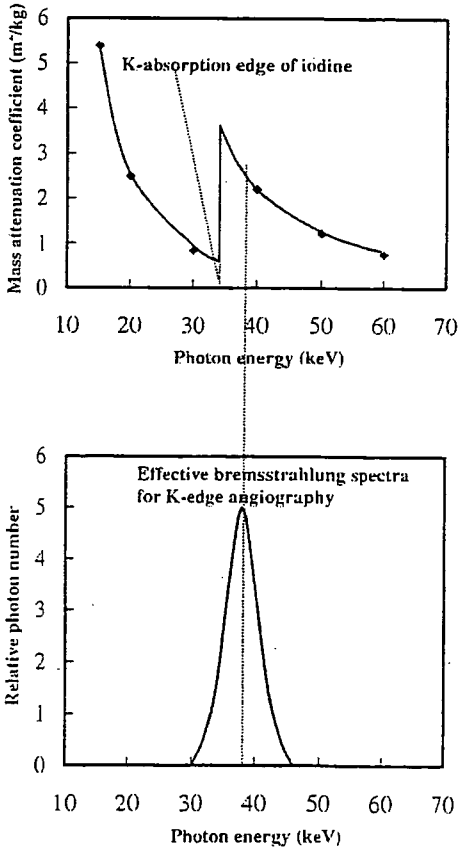


Fig. 9 Mass attenuation coefficients of iodine and effective bremsstrahlung x-rays for enhanced K-edge angiography.

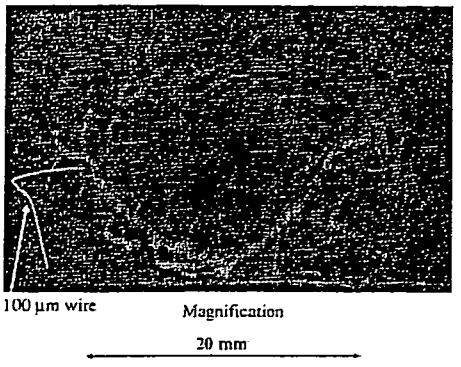


Fig. 10 Angiogram of an extracted rabbit heart using iodine microspheres.

Magnification angiography was performed at the same conditions using iodine microspheres of 15 $\mu$m in diameter. The microspheres (containing 37% iodine by weight) are very useful for making phantoms of nonliving animals used for angiography. An angiogram of a rabbit heart is shown in Fig. 10, and the coronary arteries are visible. Figure 11 shows angiograms of a larger dog heart using iodine spheres. Although the image contrast decreased slightly with increases in the thickness of the PMMA plate facing the x-ray source, coronary arteries of approximately 100 $\mu$m were observed using a 100-mm-thick plate.

## 4 Conclusion and Outlook

We employ an x-ray generator with a 100-$\mu$m-focus tungsten tube and perform enhanced K-edge magnification angiography using narrow-photon-energy bremsstrahlung x-rays with a peak photon energy of approximately 35 keV, which can be absorbed easily by iodine-based contrast me-

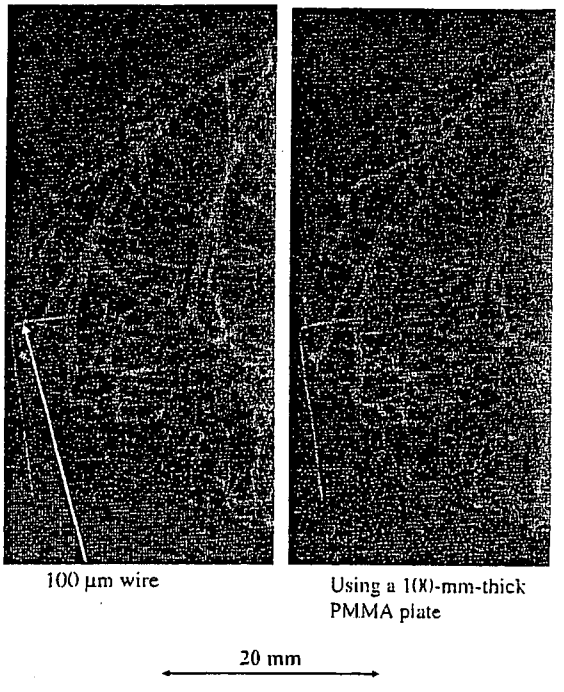


Fig. 11 Angiograms of an extracted dog heart.

dia. The bremsstrahlung x-ray intensity substantially increases with increase in the tube voltage, and the tube voltage is determined as 60 kV to increase the image contrast. In magnification angiography, although we obtain mostly absorption-contrast images, the phase-contrast effect may be added in cases where low-density media are employed.

Because the sampling pitch of the CR system is 87.5 $\mu$m, we obtain spatial resolutions of approximately 50 $\mu$m using threefold magnification imaging, even when a 100-$\mu$m-focus tube is employed. To observe fine blood vessels of less than 100 $\mu$m, the spatial resolution of the CR system should be improved to 43.8 $\mu$m (Konica Minolta Regius 190), and the iodine density should be increased. Based on experimental results, the maximum magnification rate without blurring is approximately threefold using a 100-$\mu$m-focus tube, and the rate increases with decreasing the focus diameter. In addition, the rate should be minimized to decrease the exposed dose from patients.

At a tube voltage of 60 kV and a current of 0.50 mA, the maximum number of photons was approximately $4 \times 10^7$ photons/(cm$^2$·s) at 1.0 m from the source, and the photon count rate can be increased easily using a rotating anode microfocus tube. Recently, the maximum electric power of the microfocus x-ray tube has been increasing, and the kilowatt-range tube can be realized. Furthermore, since a 10-$\mu$m-focus rotating anode tube has been developed by Hitachi Medical Corporation, dynamic high-resolution angiography is possible using a flat panel detector with a pixel size of less than 100 $\mu$m. Finally, this high-resolution, high-contrast angiography could be very useful for observing fine blood vessels in regenerative medicine, coronary arteries, and irregular capillaries in cancers.

## Acknowledgments

This work was supported by Grants-in-Aid for Scientific Research (13470154, 13877114, 16591181, and 16591222) and Advanced Medical Scientific Research from MECSST, Health and Labor Sciences Research Grants (RAMT-nano-001, RHGTEFB-genome-005, and RHGTEFB-saisei-003), grants from the Keiryo Research Foundation, The Promotion and Mutual Aid Corporation for Private Schools of Japan, Japan Science and Technology Agency (JST), and the New Energy and Industrial Technology Development Organization (NEDO, Industrial Technology Research Grant Program in 2003).

## References

1. R. Germer, "X-ray flash techniques," *J. Phys. E* **12**, 336–350 (1979).
2. E. Sato, Y. Hayasi, R. Germer, E. Tanaka, H. Mori, T. Kawai, T. Ichimaru, S. Sato, K. Takayama, and H. Ido, "Portable x-ray generator utilizing a cerium-target radiation tube for angiography," *J. Electron Spectrosc. Relat. Phenom.* **137-140**, 699–704 (2004).
3. E. Sato, E. Tanaka, H. Mori, T. Kawai, T. Ichimaru, S. Sato, K. Takayama, and H. Ido, "Demonstration of enhanced K-edge angiography using a cerium target x-ray generator," *Med. Phys.* **31**, 3017–3021 (2004).
4. E. Sato, S. Kimura, S. Kawasaki, H. Isobe, K. Takahashi, Y. Tamakawa, and T. Yanagisawa, "Repetitive flash x-ray generator utilizing a simple diode with a new type of energy-selective function," *Rev. Sci. Instrum.* **61**, 2343–2348 (1990).
5. A. Shikoda, E. Sato, M. Sagae, T. Oizumi, Y. Tamakawa, and T. Yanagisawa, "Repetitive flash x-ray generator having a high-durability diode driven by a two-cable-type line pulser," *Rev. Sci. Instrum.* **65**, 850–856 (1994).
6. E. Sato, K. Takahashi, M. Sagae, S. Kimura, T. Oizumi, Y. Hayasi, Y. Tamakawa, and T. Yanagisawa, "Sub-kilohertz flash x-ray generator utilizing a glass-enclosed cold-cathode triode," *Med. Biol. Eng. Comput.* **32**, 289–294 (1994).
7. K. Takahashi, E. Sato, M. Sagae, T. Oizumi, Y. Tamakawa, and T. Yanagisawa, "Fundamental study on a long-duration flash x-ray generator with a surface-discharge triode," *Jpn. J. Appl. Phys., Part 1* **33**, 4146–4151 (1994).
8. E. Sato, Y. Hayasi, R. Germer, E. Tanaka, H. Mori, T. Kawai, T. Ichimaru, K. Takayama, and H. Ido, "Quasi-monochromatic flash x-ray generator utilizing weakly ionized linear copper plasma," *Rev. Sci. Instrum.* **74**, 5236–5240 (2003).
9. E. Sato, Y. Hayasi, R. Germer, E. Tanaka, H. Mori, T. Kawai, T. Ichimaru, S. Sato, K. Takayama, and H. Ido, "Sharp characteristic x-ray irradiation from weakly ionized linear plasma," *J. Electron Spectrosc. Relat. Phenom.* **137-140**, 713–720 (2004).
10. E. Sato, E. Tanaka, H. Mori, T. Kawai, S. Sato, and K. Takayama, "Clean monochromatic x-ray irradiation from weakly ionized linear copper plasma," *Opt. Eng.* **44**, 049002 (2005).
11. E. Sato, M. Sagae, E. Tanaka, Y. Hayasi, R. Germer, H. Mori, T. Kawai, T. Ichimaru, S. Sato, K. Takayama, and H. Ido, "Quasi-monochromatic flash x-ray generator utilizing a disk-cathode molybdenum tube," *Jpn. J. Appl. Phys., Part 1* **43**, 7324–7328 (2004).
12. E. Sato, E. Tanaka, H. Mori, T. Kawai, T. Ichimaru, S. Sato, K. Takayama, and H. Ido, "Compact monochromatic flash x-ray generator utilizing a disk-cathode molybdenum tube," *Med. Phys.* **32**, 49–54 (2005).
13. A. Momose, T. Takeda, Y. Itai, and K. Hirano, "Phase-contrast x-ray computed tomography for observing biological soft tissues," *Nat. Med.* **2**, 473–475 (1996).
14. M. Ando, A. Maksimenko, H. Sugiyama, W. Pattanasiriwisawa, K. Hyodo, and C. Uyama, "A simple x-ray dark- and bright- field imaging using achromatic Laue optics," *Jpn. J. Appl. Phys., Part 2* **41**, L1016–L1018 (2002).
15. H. Mori, K. Hyodo, E. Tanaka, M. U. Mohammed, A. Yamakawa, Y. Shinozaki, H. Nakazawa, Y. Tanaka, T. Sekka, Y. Iwata, S. Honda, K. Umetani, H. Ueki, T. Yokoyama, K. Tanioka, M. Kubota, H. Hosaka, N. Ishizawa, and M. Ando, "Small-vessel radiography in situ with monochromatic synchrotoron radiation," *Radiology* **201**, 173–177 (1996).
16. K. Hyodo, M. Ando, Y. Oku, S. Yamamoto, T. Takeda, Y. Itai, S. Ohtsuka, Y. Sugishita, and J. Tada, "Development of a two-dimensional imaging system for clinical applications of intravenous coronary angiography using intense synchrotron radiation produced by a multipole wiggler," *J. Synchrotron Radiat.* **5**, 1123–1126 (1998).
17. E. Sato, K. Sato, T. Usuki, and Y. Tamakawa, "Film-less computed radiography system for high-speed imaging," *Ann. Rep. Iwate Med. Univ. Sch. Lib. Arts Sci.* **35**, 13–23 (2000).
18. A. Ishisaka, H. Ohara, and C. Honda, "A new method of analyzing edge effect in phase contrast imaging with incoherent x-rays," *Opt. Rev.* **7**, 566–572 (2000).
19. E. Sato, Y. Hayasi, R. Germer, E. Tanaka, H. Mori, T. Kawai, T. Ichimaru, S. Sato, K. Takayama, and H. Ido, "Portable x-ray generator utilizing a cerium-target radiation tube for angiography," *J. Electron Spectrosc. Relat. Phenom.* **137-140**, 699–704 (2004).
20. E. Sato, E. Tanaka, H. Mori, T. Kawai, T. Ichimaru, S. Sato, K. Takayama, and H. Ido, "Demonstration of enhanced K-edge angiography using a cerium target x-ray generator," *Med. Phys.* **31**, 3017–3021 (2004).

**Eiichi Sato** received his BS, MS, and PhD in applied physics from Tohoku Gakuin University, Sendai, Japan, in 1979, 1982, and 1987, respectively. He is currently a professor in the Department of Physics at Iwate Medical University. He has written some 400 publications and delivered some 200 international presentations concerning x-rays. His research interests include soft flash x-ray generators, quasi-x-ray laser generators, and high-speed radiography. In 2000, he received the Schardin Gold Medal from the German Physical Society, in 2003 he received the Takayama Award (Gold Medal) from the Japan Society of High Speed Photography and Photonics, and he received the Honorable Mention Poster Award from the SPIE International Symposium on Medical Imaging 2005.

**Etsuro Tanaka** received his MD and PhD degrees in medicine from Kumamoto University, Japan, in 1980 and 1986, respectively. He worked on medical image processing in the Department of Physiology, Tokai University, Japan, from 1988 to 2003. He is currently a professor in the Department of Nutritional Sciences, Tokyo University of Agriculture, Japan. His research interests include medical image processing, human physiology, and clinical nutrition.

**Hidezo Mori** received a medical degree from Keio University School of Medicine, Tokyo, Japan, in 1977, and also a PhD from the Post Graduate School, Keio University School of Medicine. Now he is the director of the Department of Cardiac Physiology at the National Cardiovascular Center, Suita, Japan. His primary research interests are regenerative therapy in cardiovascular disease, microcirculation, and medical applications of structural biology.

**Hiroki Kawakami** received BS and MS degrees in precision mechanics engineering from Shizuoka University in 1990 and 1992, respectively, and joined Hamamatsu Photonics K. K. in 1992. He was involved in a national project on the research and development of microangiography systems from 1999 to 2004. Now he is engaged in research and development of microfocus x-ray sources and high-resolution x-ray imaging systems.

**Toshiaki Kawai** received the BS degree in precision mechanics and the MS degree in electronic engineering from Shizuoka University, Hamamatsu, Japan, in 1964 and 1974, respectively. In 1974, he joined the Hamamatsu Photonics K. K., where he worked on the research and development of solid-state infrared detectors, and then from 1978 to 1981, he engaged in research work on the NEA cold cathode for application to imaging camera tubes. He is now the project coordinator of Electron Tube Division 2 and is engaged in the development and manufacturing of imaging devices and x-ray equipment. He is a member of the Japan Radioisotope Association and the Institute of Image Information and Television Engineers of Japan.

**Takashi Inoue** received his MD and PhD degrees in 2000 from Tohoku University. He is currently an assistant professor in the Department of Neurosurgery at Iwate Medical University, and a member of the Japan Neurosurgical Society. His research interests include neurosurgery and magnetic resonance imaging.

**Akira Ogawa** receive his MD and PhD degrees in 1981 from Tohoku University. He is currently a professor in the Department of Neurosurgery, dean of the School of Medicine at Iwate Medical University, and is a trustee of the Japan Neurosurgical Society. His research interests include neurosurgery and cerebrovascular disease.

**Mitsuru Izumisawa** graduated from Iwate Medical University, School of Dentistry, in 1992. He worked for the Department of Oral Surgery at Iwate Medical University Hospital from 1992 to 1999. He received his MD degree from Iwate Medical University in 2004. As of 2005, he is an assistant professor in the Department of Oral Radiology. His research interests include diagnostic modality and intra-arterial infusion chemotherapy for head and neck cancer.

**Kiyomi Takahashi** received her MD degree from Iwate Medical University in 1989. She worked for the Department of Neurology, Johns Hopkins University School of Medicine from 1992 to 1994. She is currently an assistant professor in the Department of Microbiology, Iwate Medical University School of Medicine. Her research interests include pathophysiology of neurological involvement in HIV and Shiga toxin-producing *E. coli* (STEC) infections, and cerebral angiography.

**Shigehiro Sato** received his MD degree from Iwate Medical University in 1980. He worked for the laboratory of the Division of Pediatric Infectious Diseases at Johns Hopkins Hospital from 1985 to 1989. He is currently a professor in the Department of Microbiology at Iwate Medical University. His research interests include central nervous system damage caused by Vero toxin, a cell culture system for vaccine development, and microangiography.

**Kazuyoshi Takayama** received his BS degree from Nagoya Institute of Technology in 1962. In 1970, he received his PhD in mechanical engineering from Tohoku University. He is currently a director (professor) in the Shock Wave Research Center, Institute of Fluid Science at Tohoku University. His research interests include various shock wave phenomena, high-speed photography, and flash radiography. He has received seven awards, including the coveted Ernst Mach Medal in 2000.

**Jun Onagawa** received his BS and PhD degrees in applied physics from Tohoku Gakuin University in 1968 and 2001, respectively. He is currently a professor in the Department of Applied Physics and Informatics, Faculty of Engineering, at Tohoku Gakuin University. His research interests include target metallography and x-ray spectroscopy.

J Pharmacol Sci 104, 341 – 348 (2007)

Journal of Pharmacological Sciences


*Full Paper*

# Edaravone Preserves Coronary Microvascular Endothelial Function After Ischemia/Reperfusion on the Beating Canine Heart In Vivo

Renan Sukmawan[1,*], Toyotaka Yada[2], Eiji Toyota[1], Yoji Neishi[1], Teruyoshi Kume[1], Yoshiro Shinozaki[3], Hidezo Mori[4], Yasuo Ogasawara[2], Fumihiko Kajiya[2], and Kiyoshi Yoshida[1]

*Departments of [1]Cardiology and [2]Medical Engineering and Systems Cardiology, Kawasaki Medical School, Kurashiki 701-0192, Japan*
*[3]Department of Physiology, Tokai University School of Medicine, Isehara 259-1193, Japan*
*[4]Department of Cardiac Physiology, National Cardiovascular Center Research Institute, Suita 565-8565, Japan*

*Received January 22, 2007; Accepted June 13, 2007*

**Abstract.** We examined whether edaravone (3-methyl-1-phenyl-2-pyrazolin-5-one), a free radical scavenger, exerts its protective effect on coronary microvessels after ischemia/reperfusion (I/R) in vivo. Ninety-minute coronary occlusion followed by reperfusion was performed in 16 open-chest dogs with and without edaravone administration. Coronary small artery (≥100 μm in size) and arteriolar (<100 μm) vasodilation, in the presence of endothelium-dependent (acetylcholine) or -independent (papaverine) vasodilators, was directly observed using intravital microscopy before and after I/R. I/R impaired microvascular vasodilation in response to acetylcholine, whereas administration of edaravone preserved the response in microvessels of both sizes, but to a greater extent in the coronary small arteries. No significant changes were noted with papaverine administration. In the edaravone group, the fluorescent intensity from reactive oxygen species (ROS) was lower, whereas nitric oxide (NO) intensity was higher relative to controls in the microvessels of the ischemic area. In conclusion, edaravone preserves coronary microvascular endothelial function after I/R in vivo. These effects, which were NO-mediated, were attributed to the ROS scavenging properties of edaravone.

***Keywords***: coronary microvessel, edaravone, ischemia/reperfusion, reactive oxygen species, nitric oxide (NO)

## Introduction

Coronary microvessels play a pivotal role in the regulation of coronary blood flow (1, 2). Dysfunction of coronary microvessels, especially the resistance vessels, has been associated with an increase in future cardiovascular events in patients with coronary diseases (3, 4). Even in normal subjects, coronary microvascular dysfunction has been shown to increase the risk for a cerebrovascular event (5).

Ischemia/reperfusion (I/R) may result in microvascular dysfunction that further attenuates cardiac functional recovery (6 – 8). One of the central mechanisms responsible for the adverse effect of I/R is free radical production, which includes reactive oxygen species (ROS) (9, 10). A burst of ROS is generated during ischemia and in early reperfusion. This burst overwhelms the antioxidant defense band and causes disturbance in the cardiovascular system (11, 12).

Edaravone (3-methyl-1-phenyl-2-pyrazolin-5-one), a potent free radical scavenger, has been shown to protect cardiomyocytes and brain against I/R injury (13, 14). However, the beneficial effects on coronary microcirculation after I/R remains unknown. We sought to define the effects of edaravone on coronary microvessels after I/R in vivo by 1) direct observation of endothelium-dependent and -independent vasodilation of subepicardial coronary microvessels on the beating canine heart using a charged couple device (CCD) intravital microscope and 2) In-situ detection of ROS and

*Corresponding author. Present address: Department of Cardiology and Vascular Medicine, University of Indonesia / National Cardiovascular Center, Jalan Letjen S Parman Kav 87, Jakarta 11420, Indonesia rey1708@yahoo.com
Publihshed online in J-STAGE
doi: 10.1254/jphs.FP0070186

nitric oxide (NO) in coronary microvessels.

## Material and Methods

*Animal preparation*

We conformed to the Guideline on Animal Experiments and the Guide for the Care and Use of Laboratory Animals published by the National Institutes of Health (NIH) of the United States and the Guiding Principles for the Care and Use of Laboratory Animals approved by the Japanese Pharmacological Society. Sixteen adult mongrel dogs of either sex (15 – 24 kg; purchased from Nagoyalab Service, Mizunami) were premedicated with ketamine (10 mg/kg, i.m.) and anesthetized with sodium pentobarbital (25 mg/kg, i.v.). Each animal was intubated and mechanically ventilated (model VS-600; Instrumental Development, Pittsburgh, PA, USA) with 2% – 3% fluorethane. Blood gas and oxygen saturation were controlled within physiologic ranges throughout the experiment. Open-chest surgery was performed by medial sternotomy and the left anterior descending artery (LAD) was isolated free from surrounding tissue at proximal and medial portions. A transonic flow probe (T206; Transonic Systems, Ithaca, NY, USA) was placed at the medial portion of the LAD to measure the coronary flow rate. A clamp was placed at the proximal LAD to produce coronary occlusion and reperfusion. Visible native collateral vessels were ligated to limit collateral flow into the ischemic area during LAD occlusion. A 6F-catheter was inserted into the right carotid artery through the left coronary artery to administer the vasodilator.

*Experimental protocols*

After instrumentation, a minimum of 30 min were allowed for stabilization while monitoring hemodynamic variables. The study protocol was as follows: i) The arteriolar vasodilatory response to endothelium-dependent (acetylcholine, 1 $\mu$g/kg, i.c.; Daiichi Pharmaceutical Co., Ltd., Tokyo) and -independent (papaverine, 1 mg, i.c.; Dainippon Sumitomo Pharma Co., Ltd., Osaka) vasodilators were examined before and after coronary I (90 min) /R (60 min) under the following conditions: a) control condition, and b) edaravone administration (3 mg/kg, i.v.; supplied by Mitsubishi Pharma Co., Ltd., Osaka) before coronary occlusion. Microspheres were administered at 85 min of coronary occlusion to measure regional myocardial blood flow (MBF). ii) Fluorescent treatment to assess microvascular ROS and NO were performed in 6 dogs (n = 3, each group) after a 60-min reperfusion period. iii) In another 10 dogs (n = 5, each), reperfusion was continued for 5 h and the infarct size and regional MBF were measured.

*Intravital CCD microscopy*

Direct observation of coronary microvascular vasodilation on the beating heart was performed by using a needle-probe intravital CCD microscope (VMS 1210; Nihon Kohden, Tokyo). It contains a gradient index lens (with a magnification of 200) surrounded by light guide fibers and a double lumen sheath. To avoid direct compression of the vessels by the needle-tip, a doughnut-shaped balloon had been installed (15). Vascular images were acquired by gently placing the needle-probe on subepicardial microvessels and were recorded at 30 frames/s. Off-line quantitative analysis was performed using an NIH image analysis software by measuring maximum diameter changes during acetylcholine or papaverine administration.

*In situ detection of ROS and NO in coronary microvessels*

After reperfusion, the heart was immediately removed. The LAD orifice and left circumflex (LCX) artery were cannulated for a continuous phosphate-buffered saline (PBS) infusion. Small tissue blocks were taken from both ischemic (LAD area) and non-ischemic regions (LCX area), and they were frozen in optimal cutting temperature compound (Tissue-Tek; Sakura Fine Chemical, Tokyo) within a few hours. Fluorescent images of the microvessels were obtained using a fluorescent microscope (Olympus BX 51; Olympus, Tokyo). Dihydroethidium (DHE; Molecular Probes, Eugene, OR, USA) and 4,5-diaminofluorescein diacetate (DAF-2DA; Daiichi Pure Chemicals, Tokyo) were used to detect ROS and NO production, respectively (16). Five regions of interest (ROI) were selected within the intimal layer of each microvessel. Fluorescent intensities of ROS and NO in the microvessels were measured by NIH software. The average value of the peak fluorescent intensity from each ROI was divided by background intensity (relative intensity) and noted as the microvascular ROS or NO intensities.

*Western blotting*

Myocardial tissue samples from the LAD and LCX area in each group were isolated for western blotting to assess endogenous NO synthase (eNOS) protein expression after I/R, as previously described (8, 16). Briefly, myocardial tissues were homogenized in the lysis buffer. After centrifugation, the supernatant was collected for immunoblotting. The proteins were transferred by semi-dry electroblotting to polyvinylidene difluoride membranes. The blots were then blocked and incubated with rabbit anti-eNOS polyclonal antibody (0.1 $\mu$g/ml; Santa Cruz Biotechnology, Santa Cruz, CA, USA) or anti-actin antibody (Santa Cruz Biotechnology) for 120 min

at room temperature. The blots were then incubated with horseradish peroxidase-conjugated goat anti-rabbit IgG (0.08 $\mu$g/ml, Santa Cruz Biotechnology). The antibody was visualized using an enhanced chemiluminescence method (ECL; Amersham Biosciences, Piscataway, NJ, USA). The integrated density of the eNOS bands was normalized by actin band density (relative density) (NIH Image).

*Regional blood flow and infarct size*

To confirm infarct size reduction by edaravone in relation to the effect of collateral flow, regional MBF was assessed by non-radioactive microspheres (Sekisui Plastic Co., Ltd., Tokyo), as previously described (17). Briefly, 1 ml of the microsphere suspension (2 to 4 $\times$ $10^6$ spheres) was injected into the left atrium 85 min after the onset of coronary occlusion. MBF was measured by assessing X-ray spectra of the fluorescent stable heavy elements using a wavelength-dispersive spectrometer (model PW 1480; Philips Co., Ltd., Eindhoven, the Netherlands). Myocardial collateral flow (ml/min per gram) was calculated using the following formula: tissue flow-rate = tissue counts $\times$ (reference flow / reference counts).

Myocardial short-axis slices (5-mm-thickness) of the left ventricle were made and incubated in 1% 2,3,5-triphenyltetrazoliumchloride solution (Sigma, Tokyo) for 10 min to identify the infarct area. Infarct size was expressed as a percentage of the infarct area relative to the area of risk (18).

*Statistical analysis*

Data are expressed as the mean $\pm$ S.E.M. The vascular response was analyzed by one-way analysis of variance followed by a Scheffe's post-hoc test for multiple comparisons (Figs. 1C, 2, 3, and 4). Regression analysis was applied in Fig. 5. Statistical significance was defined as $P<0.05$.

## Results

*Hemodynamics*

Hemodynamic data are shown in Table 1. Mean arterial pressure and heart rate during administration of acetylcholine and papaverine were not statistically different as compared to their respective baseline. Hemodynamic variables at baseline did not significantly change before and after I/R nor after edaravone administration.

*Endothelium-dependent vasodilation*

We assessed the diameter changes of 22 coronary microvessels under acetylcholine (1 $\mu$g/kg, i.c.) in each group. The diameter changes of small artery and arteriole in each group are depicted in Fig. 1, A and B. Under control conditions (without edaravone), I/R strikingly impaired endothelium-dependent vasodilation at 60 min after I/R. Meanwhile, edaravone administration augmented the response in coronary microvessels of both sizes. Preservation of vasodilation under acetylcholine was more prominent in the small artery than the arteriole. Coronary flow in the presence of acetylcholine was improved after I/R in the edaravone-adminstered group compared with that in the controls (without edaravone) (Fig. 1C).

*ROS intensity in coronary microvessels*

Fifteen coronary microvessels (<300 $\mu$m) were assessed from both the LAD and LCX areas in both groups (Fig. 2). ROS fluorescent intensity at 60 min after I/R in the microvessels from the LAD area in the control group was higher than in the LCX area ($P<0.01$). Meanwhile, ROS intensity in the microvessels from the LAD area of the edaravone group was significantly lower than that in the control group ($P<0.01$).

*Intensity of NO in coronary microvessels*

Fluorescent intensity of NO in the endothelial layer was assessed semi-quantitatively in 15 microvessels from the LAD or LCX areas in both groups 60 min after

**Table 1.** Hemodynamics data before and after ischemia/reperfusion

| | Before I/R | | | After I/R | | |
|---|---|---|---|---|---|---|
| | Baseline | Acetylcholine | Papaverine | Baseline | Acetylcholine | Papaverine |
| Mean blood pressure (mmHg) | | | | | | |
| Control | 91 ± 4 | 90 ± 6 | 91 ± 4 | 89 ± 4 | 89 ± 5 | 87 ± 5 |
| Edaravone | 92 ± 2 | 91 ± 4 | 90 ± 3 | 93 ± 3 | 91 ± 5 | 90 ± 4 |
| Heart rate (beats/min) | | | | | | |
| Control | 123 ± 5 | 125 ± 3 | 126 ± 4 | 120 ± 4 | 122 ± 5 | 120 ± 5 |
| Edaravone | 124 ± 4 | 126 ± 6 | 123 ± 5 | 123 ± 4 | 121 ± 5 | 120 ± 4 |

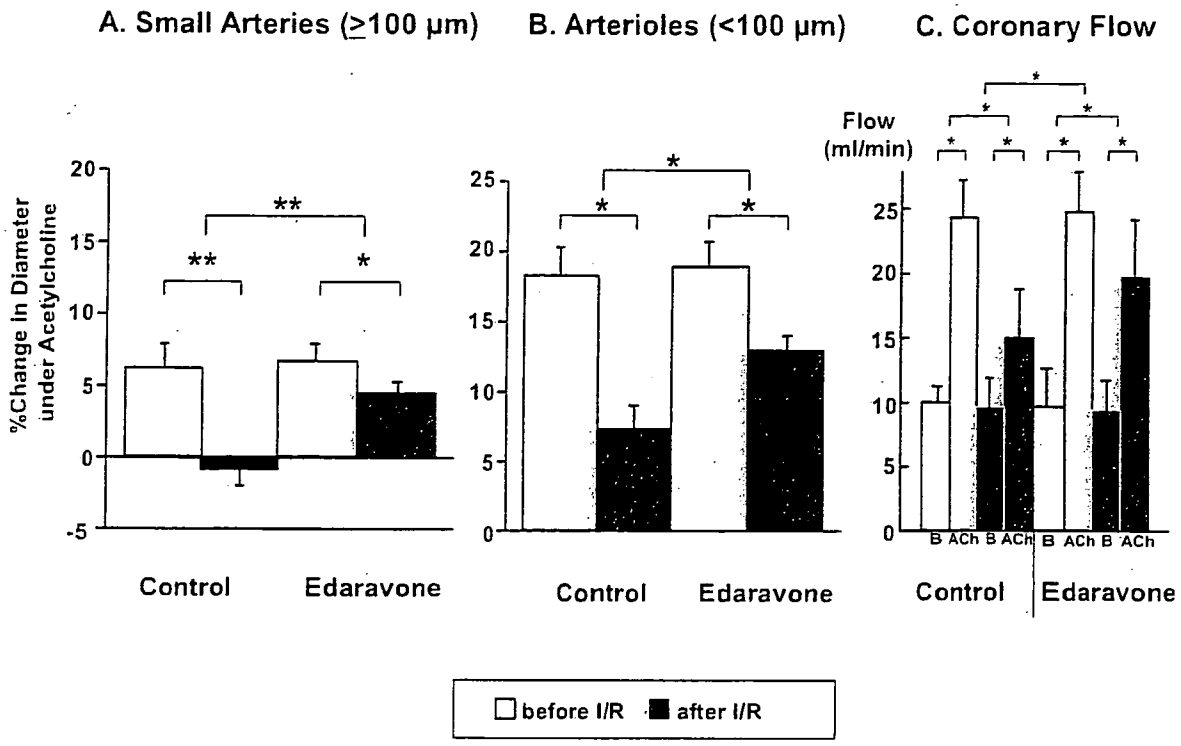


Fig. 1. Endothelium-dependent vasodilation in coronary microvessels in vivo. Edaravone administration augmented the vasodilation of small arteries (A) and arterioles (B) and improved coronary flow (C) under acetylcholine after I/R. Number of small arteries and arterioles assessed were 10 and 12, respectively. *$P$<0.05, **$P$<0.01. B = baseline, ACh = acetylcholine.

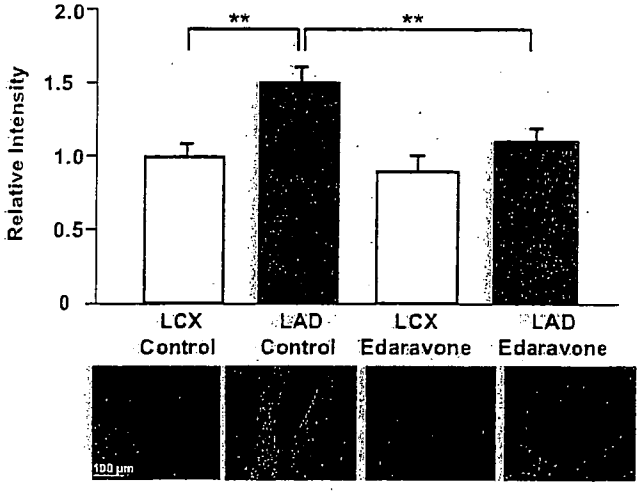


Fig. 2. In situ detection of ROS in coronary microvessels after I/R. The fluorescent intensity of ROS in microvessels from each area is shown (n = 15, in each area) with their representative DHE-fluorescence image of ROS in the vessels. **$P$<0.01.

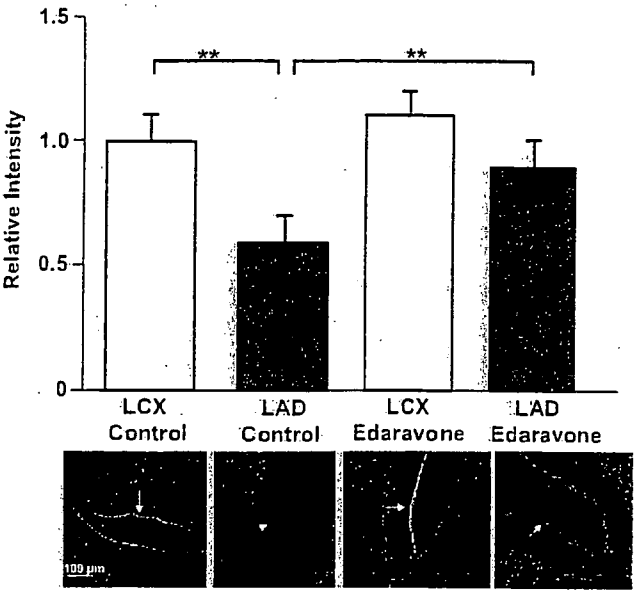


Fig. 3. In situ detection of NO in coronary microvessels after I/R. Fluorescent intensity of NO in microvessels from each area is shown (n = 15, in each area) with their representative DAF2-DA fluorescence image of NO in the endothelial layer (white arrow). **$P$<0.01.

I/R (Fig. 3). In the LAD area of the control group (without edaravone), I/R reduced the microvascular NO intensity level as compared to the LCX area ($P$<0.01). Administration of edaravone significantly preserved NO

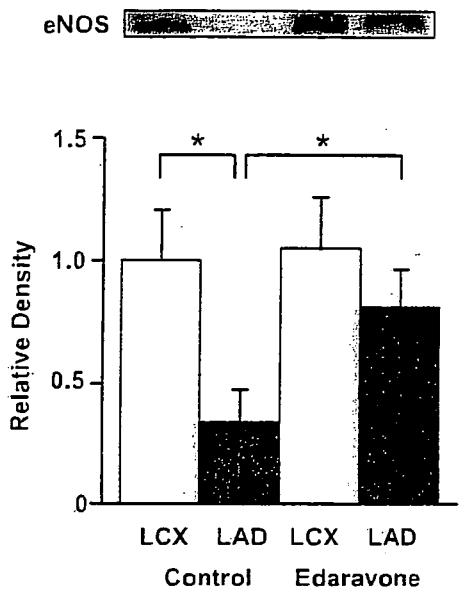


Fig. 4. eNOS protein immunoblotting after I/R. Edaravone administration augmented myocardial eNOS expression after I/R in the ischemic area. *$P$<0.05.

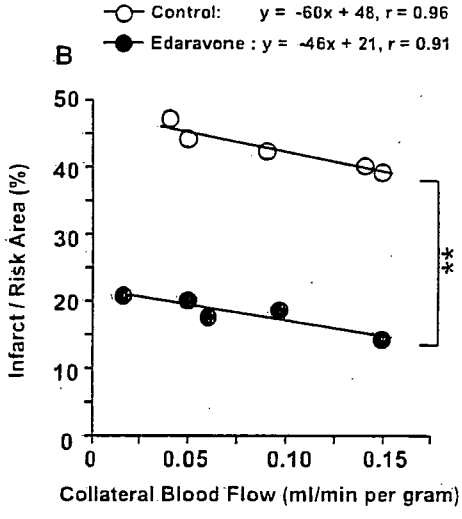


Fig. 5. Correlation of regional collateral flow and infarct size in the control and edaravone groups. **$P$<0.01.

fluorescent intensity in microvessels of LAD relative to the control group ($P$<0.01).

*Myocardial eNOS expression*

Myocardial eNOS protein expression in the LAD distribution after I/R was significantly decreased relative to the LCX area in the control group (without edaravone, $P$<0.05, Fig. 4). Edaravone augmented eNOS protein expression in the LAD area ($P$<0.05 *vs* controls).

*Collateral flow and infarct size*

There were linear negative correlations between regional collateral MBF and infarct size in the control ($y = -60X + 48$, $r = 0.96$, $P$<0.001) and edaravone ($y = -46X + 21$, $r = 0.91$, $P$<0.001) groups, which were significantly different between the 2 groups ($P$<0.01, Fig. 5). This finding indicated that the protective effect of edaravone was independent of collateral flow.

*Endothelium-independent vasodilation*

Endothelium-independent vasodilation with papaverine (1 mg, i.c.) was comparable under all conditions (Fig. 6). Administration of edaravone did not result in any significant diameter changes in small arteries and arterioles under papaverine after I/R.

## Discussion

The present study revealed that edaravone preserves endothelium-dependent vasodilation in coronary small arteries and arterioles after I/R injury on the beating canine heart in vivo by reducing ROS and thereby augmenting NO availability in the microvessels. To our knowledge, the present study is the first to report that edaravone exerts protective effects on the coronary microvascular endothelial function after I/R on the beating heart in vivo.

*Scavenging ROS by edaravone during ischemia/reperfusion*

Generation of ROS during I/R has been shown through several mechanisms such as the xanthine oxidase, mitochondrial electron transport chain, and NADPH oxidase pathways (10). In the present study, we revealed that edaravone scavenged ROS generated in coronary microvessels during I/R (Fig. 2). Previous studies have shown other beneficial effects of edaravone such as inhibition of the production of superoxide anion on the infarct rim (14), suppression of lipid peroxidation products (19), and reduction in inflammatory changes (20).

The burst of vascular ROS production following I/R led to endothelial dysfunction, which may have occurred as a result of hypoxic injury, manifested by endothelial cell swelling that results in the no reflow phenomenon within the first minutes of reperfusion (21). The ROS may also rapidly react with NO to form a toxic peroxynitric radical (i.e., $ONOO^-$) that further increases free radical accumulation resulting in endothelial injury (9). If the ischemia lasts for hours, structural changes such as edematous mitochondria in endothelial and smooth muscle cells, microvili formation on the surface of endothelial cells, and increased pinocytic activity and

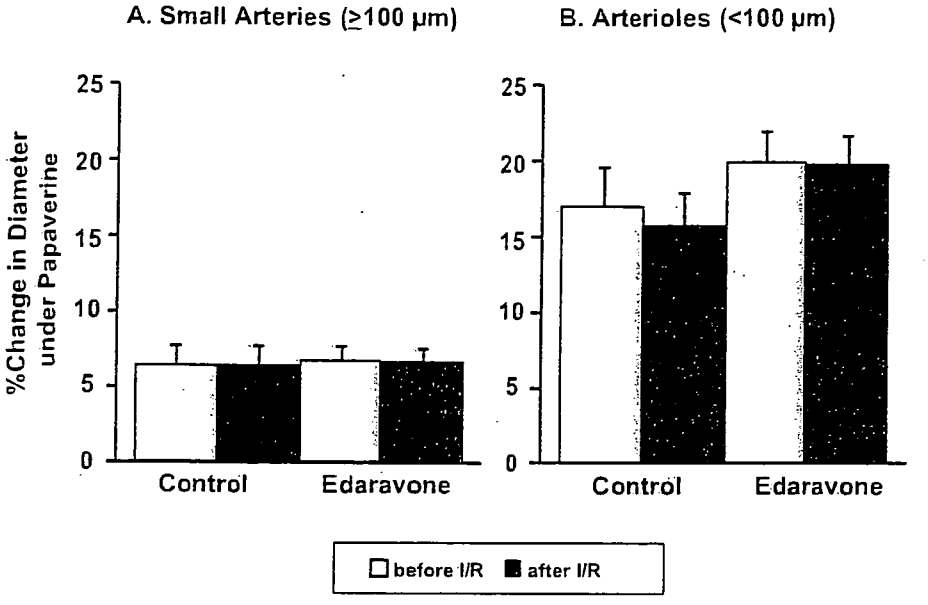


Fig. 6. Endothelium-independent vasodilation in coronary microvessels before and after I/R. The vasodilation is comparable under all conditions.

disturbed tight junctions between endothelial cells may be found by electronmicroscopical examination (21). With edaravone administration, NO bioavailability in the ischemic area endothelial layer of microvessels was significantly augmented (Fig. 3). In other settings, edaravone has also been shown to improve peripheral flow-mediated dilatation in smokers (22). Taken together, free radical scavenging by edaravone in the vessels results in preservation of NO availability and thereby maintains endothelial function, which is crucial for the cardiovascular system in both the short-term and long-term.

*Edaravone preserves nitric oxide and eNOS*

We have previously shown that endothelium-dependent vasodilation by acetylcholine would increase NO release in coronary circulation, indicating the central role of NO (23). However, the regulation of coronary vascular tone may be mediated, not only by NO, but also by the endothelium derived hyperpolarizing factor (EDHF) and adenosine (24). Yada et al. have demonstrated that endogeneous $H_2O_2$, an EDHF, and rho-kinase inhibition mediated coronary vasodilation to a greater extent in arterioles than in small arteries (7, 8, 24). In the present study, preservation of endothelium-dependent vasodilation by edaravone was noted to a greater extent in the small arteries (Fig. 1). These facts revealed various mechanisms and 'site-specific' action of different drugs or agents in the coronary circulation. These also indicated a predominant role of NO in small arteries, as opposed to arterioles. Taken together, the protective effects of NO and EDHF in coronary microvessels during I/R may occur in a compensatory manner.

Most of the NO production in the normal heart is accounted for by the presence of nitric-oxide synthase (eNOS) in the coronary endothelium and myocardium. Impaired NO synthesis from eNOS is a mechanism of endothelial dysfunction in the post-ischemic heart. The present study demonstrated reduced eNOS protein expression in the ischemic myocardium after I/R, whereas edaravone administration preserved the expression (Fig. 4). Previous studies from our institution have also demonstrated a decrease in eNOS protein expression in ischemic myocardium following I/R (7, 8). An in vitro study in HUVEC has shown that edaravone may increase eNOS expression via the inhibition of LDL oxidation (25). Thus, the burst of ROS generation during I/R may cause cell injury that results in reduced eNOS production, and edaravone administration preserves the eNOS expression.

*Myocardial protection by edaravone*

The present study confirmed the protective effect of edaravone on the myocardial cell (13) and revealed that the cardioprotective role of edaravone during I/R was irrespective of transmural collateral flow to the ischemic area (Fig. 5). It has been hypothesized that maintenance of endothelium-dependent dilation of coronary microvessels could enhance reperfusion damage and reduces the amount of tissue necrosis (26). Thus, preservation of microvascular endothelial function

by edaravone probably contributed to the improvement in myocardial perfusion, thereby facilitating myocardial tissue preservation after I/R.

In the present study, we administered edaravone prior to coronary occlusion because ROS generation may occur during occlusion and after reperfusion. Wu et al. have shown a protective effect of edaravone on the myocardium when it was administered during coronary occlusion or after reperfusion (27). Thus, we presumed that preservation of endothelial function by edaravone may also be observed if it is administered during occlusion or after reperfusion. Nevertheless, further study is needed to confirm these issues.

*Conclusions*

In conclusion, edaravone exerts beneficial protective effects on coronary microvessels by preserving endothelial function after I/R in vivo. These effects are attributed to the ROS scavenging properties of edaravone and involves an NO-mediated mechanism.

## Acknowledgments

This work was supported in part by a grant (No 16300164) from the Japanese Ministry of Education, Science, Sports, Culture, and Technology and a grant from the program for promotion of fundamental studies in health sciences of the Organization for Pharmaceutical Safety and Research in Japan.

## References

1 Chilian WM, Kuo L, DeFily DV, Jones CJ, Davis MJ. Endothelial regulation of coronary microvascular tone under physiological and pathophysiological conditions. Eur Heart J. 1993;1 Suppl 1:55–59.

2 Kuo L, Davis MJ, Chilian WM. Endothelium-dependent, flow-induced dilation of isolated coronary arterioles. Am J Physiol. 1990;259:1063–1170.

3 Suwaidi JA, Hamasaki S, Higano ST, Nishimura RA, Holmes DR, Lerman A. Long-term follow-up of patients with mild coronary artery disease and endothelial dysfunction. Circulation. 2000;101:948–954.

4 Schächinger V, Britten B, Zeiher AM. Prognostic impact of coronary vasodilator dysfunction on adverse long-term outcome of coronary heart disease. Circulation. 2000;101:1899–1906.

5 Targonski PV, Bonetti PO, Pumper GM, Higano ST, Holmes DR, Lerman A. Coronary endothelial dysfunction is associated with an increased risk of cerebrovascular events. Circulation. 2003;107:2805–2809.

6 Matsumura K, Jeremy RW, Schaper J. Progression of myocardial necrosis during reperfusion of ischemic myocardium. Circulation. 1998;97:795–804.

7 Yada T, Shimokawa H, Hiramatsu O, Kajita T, Shigeto F, Tanaka E, et al. Beneficial effect of hydroxyfasudil, a specific Rho-kinase inhibitor, on ischemia/reperfusion injury in canine coronary microcirculation in vivo. J Am Coll Cardiol. 2005;45:599–607.

8 Yada T, Shimokawa H, Hiramatsu O, Haruna Y, Morita Y, Kashihara N, et al. Cardioprotective role of endogenous hydrogen peroxide during ischemia-reperfusion injury in canine coronary microcirculation in vivo. Am J Physiol Heart Circ Physiol. 2006;291:H1138–1146.

9 Bolli R, Jeroudi MO, Patel BS, DuBose CM, Lai EK, Roberts R, et al. Direct evidence that oxygen-derived free radicals contribute to postischemic myocardial dysfunction in the intact dog. Proc Natl Acad Sci U S A. 1989;86:4695–4699.

10 Zweier JL, Talukder MA. The role of oxidants and free radicals in reperfusion injury. Cardiovasc Res. 2006;70:181–190.

11 Becker LB, vanden Hoek TL, Shao ZH, Li CQ, Schumacker PT. Generation of superoxide in cardiomyocytes during ischemia before reperfusion. Am J Physiol. 1999;277:H2240–H2246.

12 Kevin LG, Camara AK, Riess ML, Novalija E, Stowe DF. Ischemic preconditioning alters real-time measure of $O_2$ radicals in intact hearts with ischemia and reperfusion. Am J Physiol Heart Circ Physiol. 2003;284:H566–H574.

13 Yamawaki M, Sasaki N, Shimoyama M, Miake J, Ogino K, Igawa O, et al. Protective effect of edaravone against hypoxia-reoxygenation injury in rabbit cardiomyocytes. Br J Pharmacol. 2004;142:618–626.

14 Shichinohe H, Kuroda S, Yasuda H, Ishikawa T, Iwai M, Horiuchi M. Neuroprotective effects of the free radical scavenger edaravone (MCI-186) in mice permanent focal brain ischemia. Brain Res. 2004;1029:200–206.

15 Yada T, Hiramatsu O, Kimura A, Goto M, Ogasawara Y, Tsujioka K. In vivo observation of subendocardial microvessels of the beating porcine heart using a needle-probe videomicroscope with a CCD camera. Circ Res. 1993;72:939–946.

16 Satoh M, Fujimoto S, Haruna Y, Arakawa S, Horike H, Komai N, et al. NAD(P)H oxidase and uncoupled nitric oxide synthase are major sources of glomerular superoxide in rats with experimental diabetic nephropathy. Am J Physiol Renal Physiol. 2005;288:F1144–F1152.

17 Mori H, Haruyama S, Shinozaki Y, Okino H, Iida A, Takanashi R, et al. New nonradioactive microspheres and more sensitive X-ray fluorescence to measure regional blood flow. Am J Physiol Heart Circ Physiol. 1992;263:H1946–H1957.

18 Ogita H, Node K, Asanuma H, Sanada S, Takashima S, Asakura M. Amelioration of ischemia- and reperfusion-induced myocardial injury by the selective estrogen receptor modulator, raloxifene, in the canine heart. J Am Coll Cardiol. 2002;40:998–1005.

19 Zhang N, Komine-Kobayashi M, Tanaka R, Liu M, Mizuno Y, Urabe T. Edaravone reduces early accumulation of oxidative products and sequential inflammatory responses after transient focal ischemia in mice brain. Stroke. 2005;36:2220–2225.

20 Nimata M, Okabe TA, Hattori M, Yuan Z, Shioji K, Kishimoto C. MCI-186 (edaravone), a novel free radical scavenger, protects against acute autoimmune myocarditis in rats. Am J Physiol Heart Circ Physiol. 2005;289:H2514–H2518.

21 Szocs K. Endothelial dysfunction and reactive oxygen species production in ischemia/reperfusion and nitrate tolerance. Gen Physiol Biophys. 2004;23:265–269.

22 Jitsuiki D, Higashi Y, Goto C, Kimura M, Noma K, Hara K, et al. Effect of edaravone, a novel free radical scavenger, on

endothelium-dependent vasodilation in smokers. Am J Cardiol. 2004;94:1070–10703.

23 Neishi Y, Mochizuki S, Miyasaka T, Kawamoto T, Kume T, Sukmawan R, et al. Evaluation of bioavailability of nitric oxide in coronary circulation by direct measurement of plasma nitric oxide concentration. Proc Natl Acd Sci U S A. 2005;102:11456–11461.

24 Yada T, Shimokawa H, Hiramatsu O, Kajita T, Shigeto F, Goto M, et al. Hydrogen peroxide, an endogenous endothelium-derived hyperpolarizing factor, plays an important role in coronary autoregulation in vivo. Circulation. 2003;107:1040–1045.

25 Yoshida H, Sasaki K, Namiki Y, Sato N, Tada N. Edaravone, a novel radical scavenger, inhibits oxidative modification of low-density lipoprotein (LDL) and reverses oxidized LDL-mediated reduction in the expression of endothelial nitric oxide synthase. Atherosclerosis. 2005;179:97–102.

26 DeFily DV, Chilian WM. Preconditioning protects coronary arteriolar endothelium from ischemia-reperfusion injury. Am J Physiol. 1993;265:H700–H706.

27 Wu TW, Zeng LH, Wu J, Fung KP. Myocardial protection of MCI-186 in rabbit ischemia-reperfusion. Life Sci. 2002;71: 2249–2255.

FEBS Letters 581 (2007) 5859–5864

# Crystal structure of RVV-X: An example of evolutionary gain of specificity by ADAM proteinases

Soichi Takeda*, Tomoko Igarashi, Hidezo Mori

*Department of Cardiac Physiology, National Cardiovascular Center Research Institute, 5-7-1 Fujishiro-dai, Suita, Osaka 565-8565, Japan*

Received 2 November 2007; revised 21 November 2007; accepted 21 November 2007

Available online 3 December 2007

Edited by Hans Eklund

**Abstract** **Russell's viper venom factor X activator (RVV-X) is a heterotrimeric metalloproteinase with a mammalian ADAM-like heavy chain and two lectin-like light chains. The crystal structure of RVV-X has been determined at 2.9 Å resolution and shows a hook-spanner-wrench-like architecture, in which the metalloproteinase/disintegrin region constitutes a hook, and the lectin-like domains constitute a handle. A 6.5 nm separation between the catalytic site and a putative exosite suggests a docking model for factor X. The structure provides a typical example of the molecular evolution of multi-subunit proteins and insights into the molecular basis of target recognition and proteolysis by ADAM/adamalysin/reprolysin proteinases.**


*Keywords:* Metalloproteinase; Disintegrin; ADAM; Factor X activator; Snake venom; Reprolysin

## 1. Introduction

Blood coagulation factor X is a serine proteinase and is one of the key components of the hemostatic system [1]. In circulation, factor X exists as a zymogen and is converted to an active form, factor Xa, by cleavage of a single peptide bond between Arg194 and Ile195. This removes the heavily glycosylated first 52 amino terminal residues (AP: active peptide) of the heavy chain, resulting in exposure of the active site. Factor Xa in turn converts prothrombin to thrombin, which ultimately leads to formation of hemostatic plugs.

Venom from Russell's viper, *Daboia russelli*, has been recognized for its potent coagulation activity. Russell's viper venom factor X activator (RVV-X) is a well-characterized metalloproteinase which specifically activates factor X by cleaving the same Arg-Ile bond in factor X that is cleaved by factors IXa and VIIa during physiological coagulation [2,3]. RVV-X belongs to the P-IV class of snake venom metalloproteinases [4] and consists of a heavy chain of 57,600 Da and two light chains of 19,400 and 16,400 Da, linked by disulfide bonds [2,5,6]. The 427-residue heavy chain contains the metalloproteinase (M)/disintegrin (D)/cysteine-rich (C) domains [4,7] that are shared by the (ADAM) (a disintegrin and metalloproteinase)/adamalysin/reprolysin family proteins. ADAMs are membrane-anchored glycoproteins that can proteolytically release cell-surface-protein ectodomains, including cell adhesion molecules, growth factor precursors and their receptors, and have been associated with numerous diseases including rheumatoid arthritis, Alzheimer's disease, heart disease, and cancer [8,9]. The light chains of RVV-X share amino acid sequence homology with mammalian C-type ($Ca^{2+}$-dependent) lectins and C-type lectin-like proteins (CLPs) isolated from various snake venoms [7,10]. RVV-X is one of the best examples of an exogenous activators used in coagulation research and has also been frequently used in diagnostic applications [2]. However, the molecular mechanism by which RVV-X recognizes and cleaves factor X is poorly understood, primarily due to the lack of three-dimensional structural information.

We recently determined the three-dimensional structure of the metalloproteinase/disintegrin/cysteine-rich (MDC) domains of ADAM/adamalysin/reprolysin family protein VAP1 and suggested a potential protein–protein interaction site that may function in specifying target proteins [11]. Among the family proteins, RVV-X is unique in having CLP domains within the molecule and a strict substrate specificity. To extend our understanding of the protein–protein interactions and target specificity of this family of proteins, we determined the crystal structure of RVV-X. Here, we report the crystal structure of RVV-X at 2.9 Å resolution and present a factor X docking model.

## 2. Materials and methods

RVV-X was purchased from Enzyme Research Laboratories Inc. and was further purified using a CM Hi-Trap column (GE healthcare Bio-Science Corp.) in the presence of GM6001 (*N*-[(2*R*)-2-(hydroxamidocarbonyllethyl)-4-methylpentanoyl]-L-tryptophan methylamide (CALBIOCHEM)). Crystals were obtained by the sitting drop vapor diffusion method. Droplets were prepared by mixing 1 μl of protein solution and 1 μl of reservoir solution (0.1 M calcium acetate, 0.1 M sodium cacodylate, 10% PEG8000, pH 6.5) supplemented with one fifth volume of 10% PEG3350 and were equilibrated against 1 ml of reservoir solution at 293 K, typically for one week. Crystals were soaked in reservoir solution supplemented with 15% MPD (2-methyl-2,4-pentandiol) prior to flash cryo-cooling under a stream of nitrogen gas at 100 K.

The diffraction data set was acquired using the SPring-8 beamline BL41XU at a wavelength of 1.0 Å at 100 K. The best crystal generated a data set with a 2.9 Å resolution (Table 1). The asymmetric unit contained one RVV-X molecule. The RVV-X structure was solved by the molecular replacement method using search models constructed from acutolysin-C (1QUA), catrocollastatin/VAP2B (2DW0), and fIX-bind-

*Corresponding author. Fax: +81 6 6872 7485.
*E-mail address:* stakeda@ri.ncvc.go.jp (S. Takeda).

*Abbreviations:* RVV-X, Russell's viper venom factor X activator; ADAM, a disintegrin and metalloproteinase; MDC, metalloproteinase/disintegrin/cysteine-rich; HVR, hyper-variable-region; PEG, polyethyleneglycol

0014-5793/$32.00 
doi:10.1016/j.febslet.2007.11.062

Table 1
Data collection and refinement statistics

| | Crystal 1 |
|---|---|
| *Data collection* | |
| Space group | $P2_12_12_1$ |
| Cell dimensions | |
| *a*, *b*, *c* (Å) | 70.4, 91.7, 152.9 |
| $\alpha$, $\beta$, $\gamma$ (°) | 90, 90, 90 |
| Resolution (Å) | 50–2.9 (3.0–2.9) |
| $R_{merge}$[a] | 0.069 (0.212) |
| $I/\sigma I$ | 17.0 (7.0) |
| Completeness (%) | 96.4 (79.5) |
| Redundancy | 6.3 (5.5) |
| *Refinement* | |
| Resolution (Å) | 44.6–2.91 (3.0–2.91) |
| No. reflections | 21482 (1661) |
| $R_{work}$[b]/$R_{free}$[c] | 0.218/0.273 |
| No. atoms | |
| Protein | 5300 |
| $Zn^{2+}$ | 1 |
| $Ca^{2+}$ | 5 |
| carbohydrate | 106 |
| GM6001 | 28 |
| R.m.s deviations | |
| Bond lengths (Å) | 0.0045 |
| Bond angles (°) | 1.12 |

Highest resolution shell is shown in parenthesis.
[a] $R_{merge} = \sum_{hkl}\sum_i|I_i(hkl) - \langle I(hlk)\rangle|/\sum_{hkl}\sum_i I_i(hkl)$, where $I_i(hkl)$ is the *i*th intensity measurement of reflection *hkl* and $\langle I(hlk)\rangle$ is its average.
[b] $R_{work} = \sum(||F_{obs}| - |F_{calc}||)/\sum|F_{obs}|$.
[c] $R_{free}$ = *R*-value for a randomly selected subset (5%) of the data that were not used for minimization of the crystallographic residual.

ing protein (IX-bp, 1J34), for the M, C and CLP domains, respectively. The final model includes amino acid residues 7-422 of the heavy chain, 1-59 and 64-133 of light chain-A (LA) and 3-123 of light chain-B (LB), and was refined to a resolution of 2.9 Å (Table 1). The overall resolution is not particularly high when compared to those of the other snake venom protein structures, most likely due to the relatively high solvent content of the crystal (~60%) and the flexible modular architecture of the MDC domains [12]. However, well-determined structural models for most sub-domains generated the electron-density maps that enable us to build a reliable model. The overall B-factor is relatively high (average B-factor of the total protein atoms is 72.2 $Å^2$) and the electron-densities associated with the charged side-chains located on the molecular surface (61 aa corresponding to 9% of the total model of 672 aa) are not clearly observed, however, almost all of the side-chains inside the molecule are defined in the final electron-density maps (Fig. 1B and C). Details of preparation, crystallization and structural analysis are described in the Supplementary information.

## 3. Results and discussion

### 3.1. Overall structure of RVV-X

The overall structure of RVV-X resembles a hook-spanner-wrench configuration, where the major portion of the heavy chain forms a hook and the remaining heavy chain portion and the light chains form a handle (Fig. 1A). The backbone structure of the heavy chain is essentially the same as each monomer of VAP1 [11] and catrocollastain/VAP2B [12], with the exception of the sub-domain orientations (Fig. 1D and E). There are direct, but less-specific interactions between the M and C domains, most likely resulting from crystal packing forces, such that the entire RVV-X MDC domain forms a closed C-shape structure, unlike the open C-shaped structures of VAP1 and catrocollastain/VAP2B. The M domain of RVV-X has a flat elliptical shape with a core formed by a five-stranded β-sheet and five α-helices and contains the conserved $Zn^{2+}$-binding HEXXHXXGXXHD sequence (residues 145–156) and a "Met-turn" (Met169) bearing the typical structural features of the metzincin family of metalloproteinases [13]. RVV-X has a fourth disulfide bridge (Cys27-Cys63) (Fig. 1B), in addition to the three conserved disulfide bridges (Cys120-Cys200, Cys160-Cys184 and Cys162-Cys167) [4] in the M domain. The M domain is followed by the D and C domains, which are further divided into shoulder ($D_s$), arm ($D_a$), wrist ($C_w$) and hand ($C_h$), segments, and the entire heavy chain folds into a C-shaped structure (Fig. 1A). The heavy chain contains three structural $Ca^{2+}$-binding sites and a number of disulfide bridges (9 and 5 in the D and C domains, respectively) that are highly conserved among the ADAM/adamalysin/reprolysin family proteins [11,12].

The two homologous light chains have a fold similar to the carbohydrate-recognition domain (CRD) of rat mannose binding protein (MBP) [14], but they form an intertwined dimer where the central portion of each chain projects toward the adjoining subunit (Fig. 1A). The light chains are related by a pseudo 2-fold axis which is perpendicular to the long axis of the light chain dimer.

### 3.2. (HVR)-mediated protein–protein interaction

RVV-X has a unique cysteine residue (Cys389) in the middle of the hyper-variable-region (HVR, residues 373–394) in $C_h$, a putative protein–protein interaction site for this family of proteins [11]. Cys389 forms a disulfide bond with the C-terminal cysteine residue (Cys133) of LA (Fig. 1A and C). Aside from this inter-chain disulfide bridge, Tyr346, Tyr347, and Met385 in the heavy chain form multiple hydrophobic interactions and hydrogen bonds with Tyr11, Phe12, and Pro131 in LA, which further stabilize the continuous $C_h$/LA structure (Fig. 1C). Most of these residues involved in the interaction between $C_h$ and LA are not conserved among ADAMs [11,12] or among other CLPs [10]. The RVV-X structure represents the first example of HVR-mediated protein–protein interactions by the ADAM/adamalysin/reprolysin family proteins.

### 3.3. Light chains

Both the overall structure and the surface features of the RVV-X light chains are quite similar to those of the factor X-binding protein (X-bp) from *Deinagkistrodon acutus* venom (the r.m.s. deviation of the 240 equivalent Cα atoms is 2.6 Å) determined in complex with the γ-carboxyglutamic acid (Gla) domain of factor X [15] (Fig. 2A and B). X-bp has strong anticoagulant activities because it binds to the Gla domain of factor X and inhibits its membrane-anchoring function [16]. The hydrophobic residues that are critical for the membrane-anchoring function of factor X (Phe4, Leu5 and Val8) interact with the hydrophobic patch formed by the hydrophobic residues (Met113, Ile114 and Ala115) of the B chain in X-bp [15]. Those residues are conserved in RVV-X (Phe114, Ile115 and Ala116 of LB) (Fig. 2B). The positively charged patches on X-bp that directly interact with the Gla residues in factor X are conserved, but, are less prominent in RVV-X because of amino acid substitutions (especially, Ile101 and Glu104) (Fig. 2B). The structural similarities between the RVV-X light chains and X-bp suggest the intriguing possibility that RVV-X recognizes the factor X Gla domain through an exosite, formed by the light chains (Fig. 2C).

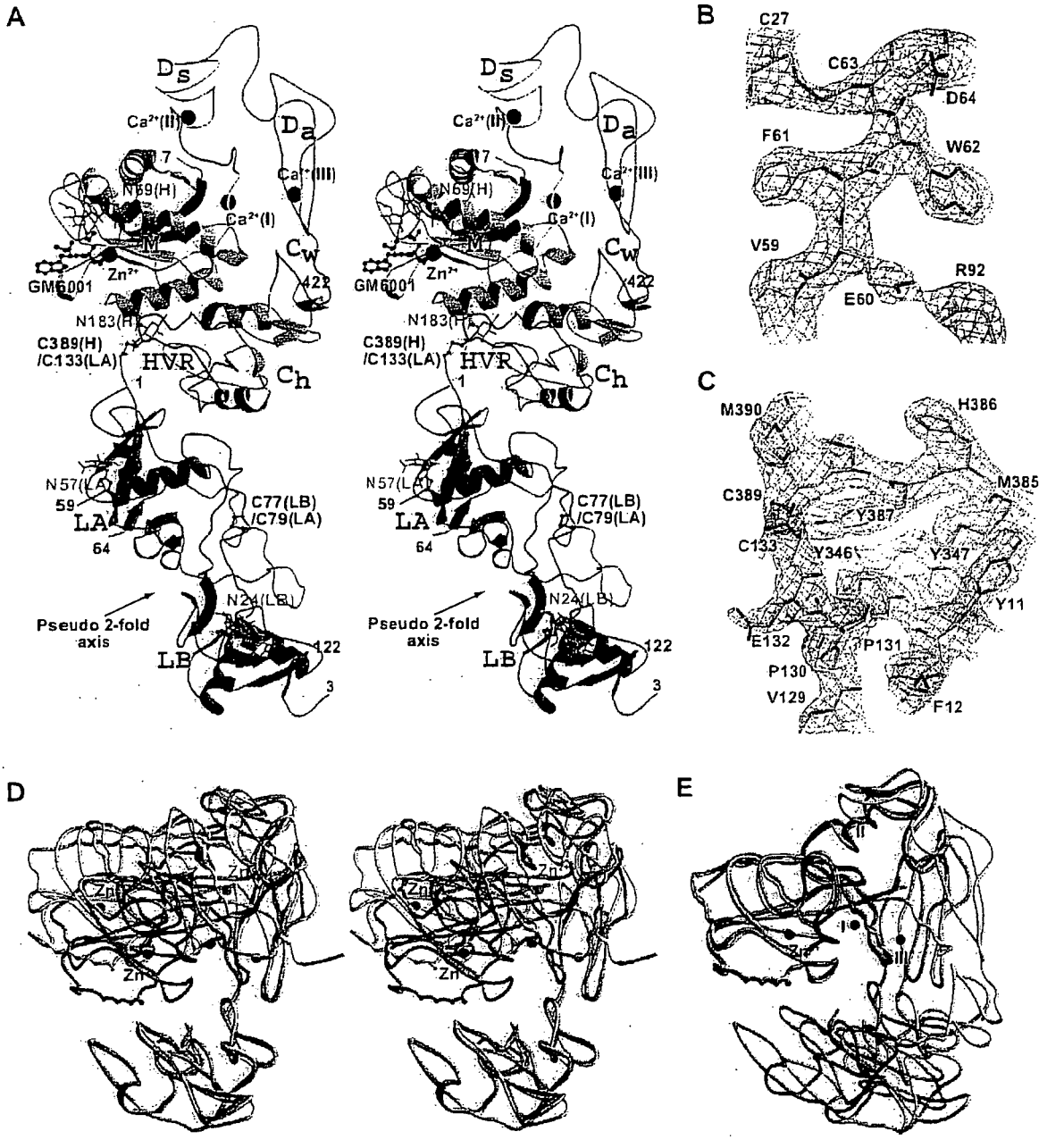


Fig. 1. Structure of RVV-X. (A) Ribbon structure of RVV-X in stereo. Bound calcium and zinc ions are represented by black and red spheres, respectively. The carbohydrate moieties (in green) linked to asparagine residues and GM6001 (in magenta) are shown in ball-and-stick representations. $2F_o - F_c$ electron-density maps ($1.0\sigma$) around the disulfide bridge between Cys27(HC) and Cys63(HC), and between Cys389 (HC) and Cys133 (LA) are represented in (B) and in (C), respectively. The HC and LA residues are labelled in black and in red, respectively. (D) Superimposition of the $C_h$ segment of the RVV-X heavy chain (in pink) with that of the VAP1 monomer (chain-A in 2ERO, in yellow), and with that of the catrocollastatin/VAP2B (chain-A in 2DW0, in cyan) in stereo. The bound zinc and calcium atoms in RVV-X are shown as red and black spheres, respectively. The zinc atoms in VAP1 and catrocollastatin/VAP2B are shown as green and blue spheres, respectively. (E) Superimposition of the M domain of the RVV-X heavy chain with the M domains of the VAP1 monomer and catrocollastatin/VAP2B.

When a properly folded Gla domain is absent from factor X, the rate of factor X activation by RVV-X is markedly diminished. In the acarboxy factor X, in which Gla formation has been blocked by a vitamin K antagonist [17] or the Des (1-44) factor X [18], factor X activation occurs at less than 1% of the rate of native factor X. Activation of factor X by RVV-X is dramatically enhanced by millimolar $Ca^{2+}$, which induces a conformational change in the Gla domain that enhances its binding to RVV-X [19]. Moreover, RVV-X catalyzed factor X activation is inhibited by X-bp [7]. Collectively, these observations suggest that the concave cleft created between the two light chains in RVV-X may function as an exosite for factor X-binding.